



Research article

Hydrogen absorption and desorption properties of Li-Mg-Al-Ti-*M* based lightweight high entropy alloys



Hirotada Hashimoto ^{a,*}, Shigehito Isobe ^{b,*}, Tatsuya Minami ^a, Kohta Asano ^c, Kouji Sakaki ^c, Naoyuki Hashimoto ^b, Hiroshi Oka ^b

^a Graduate School of Engineering, Hokkaido University, N-13, W-8, Sapporo 060-8628, Japan

^b Faculty of Engineering, Hokkaido University, N-13, W-8, Sapporo 060-8628, Japan

^c Energy Process Research Institute, National Institute of Advanced Industrial Science and Technology (AIST), Tsukuba West, 16-1 Onogawa, Ibaraki, Tsukuba 305-8569, Japan

ARTICLE INFO

ABSTRACT

Key words:

High entropy alloys
Lightweight alloys
Mechanical alloying
Hydrogen storage alloys

The hydrogen absorption and desorption properties of the Li-Mg-Al-Ti-V and Li-Mg-Al-Ti-Nb lightweight high entropy alloys (HEAs) synthesized by mechanical alloying were investigated to develop hydrogen storage alloys with high gravimetric capacity. An equiatomic $\text{Li}_{20}\text{Mg}_{20}\text{Al}_{20}\text{Ti}_{20}\text{V}_{20}$ consists of two phases; a Ti-V based body-centered cubic (BCC) phase and a Li-Mg based BCC phase. The alloy absorbs hydrogen up to $\text{H/M} = 0.74$ (2.3 wt% H_2) at 250 °C, although the hydrogen absorption and desorption induced phase separation of Mg from the Li-Mg based BCC phase. The hydrogen absorption and desorption properties of each $\text{Li}_8\text{Mg}_8\text{Al}_{28}\text{Ti}_{28}\text{V}_{28}$ and $\text{Li}_8\text{Mg}_8\text{Al}_{28}\text{Ti}_{28}\text{Nb}_{28}$ single BCC phases were also investigated. At room temperature, they absorbed hydrogen up to $\text{H/M} = 0.43$ (1.1 wt% H_2) and $\text{H/M} = 0.68$ (1.4 wt% H_2), respectively. Unlike $\text{Li}_{20}\text{Mg}_{20}\text{Al}_{20}\text{Ti}_{20}\text{V}_{20}$, no clear phase separation was observed in these alloys after hydrogen absorption and desorption.

1. Introduction

Hydrogen storage alloys safely store hydrogen in the solid state with a small volume and little energy loss [1,2]. However, it is not appropriate to use hydrogen storage alloys for a hydrogen tanks in fuel cell vehicles because of their low gravimetric capacities. Hydrogen storage alloys, such as LaNi_5 and TiFe , are mainly used in stationary applications such as the storage of hydrogen generated from renewable energy sources. However, some alloys, such as Mg-based alloys, have a high gravimetric capacity for hydrogen. To date, Mg-based alloys have been researched and developed; however, there are still problems with their poor kinetics for application in fuel cell vehicles [3,4]. To achieve appropriate hydrogen storage alloys for hydrogen tanks in fuel cell vehicles, it is necessary to develop hydrogen storage alloys with not only a high gravimetric capacity for hydrogen but also superior kinetics. Therefore, it is expected that novel hydrogen storage alloys, that can be operated at moderate temperatures with a high gravimetric capacity for hydrogen will be developed to apply hydrogen storage alloy to a hydrogen tanks in fuel cell vehicles.

In recent years, solid-solution alloys called high entropy alloys (HEAs), have attracted attention in many fields owing to their unique properties [5–7]. HEAs are composed of multiple elements, typically five or more, with similar equiatomic ratios. They are thermodynamically stable in the solid solution phase, which is attributed to their high mixing entropies. The unique properties of HEAs have been reported in the field of hydrogen storage. Despite the consensus that the maximum hydrogen content of conventional body centered cubic (BCC) alloys is $\text{H/M} = 2$, an HEA with a BCC structure consisting of Ti, V, Zr, Nb, and Hf has exceeded $\text{H/M} = 2$ at 299 °C [8]. This high hydrogen absorption capacity is attributed to large lattice distortions specific to HEAs [8]. However, it was also reported that the amount of lattice distortion in HEAs does not correlate with their hydrogen absorption capacity [9]. Although the relationship between the lattice distortion of HEAs and the hydrogen absorption capacity is still under discussion [10], a higher hydrogen storage capacity can be expected. The alloy design of HEAs for hydrogen storage have been carried out to explore the vast composition range by several method, for instance, conventional alloy design as typified by alloying hydride and non-hydride forming elements,

* Corresponding authors.

E-mail addresses: h.hashimoto@eng.hokudai.ac.jp (H. Hashimoto), isobe@eng.hokudai.ac.jp (S. Isobe), k.asano@aist.go.jp (K. Asano), kouji.sakaki@aist.go.jp (K. Sakaki), hashimoto@eng.hokudai.ac.jp (N. Hashimoto), hiroshi_oka@eng.hokudai.ac.jp (H. Oka).

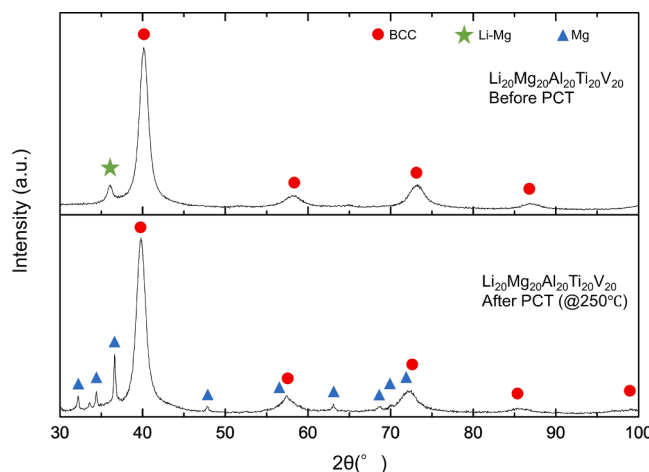


Fig. 1. XRD patterns of $\text{Li}_{20}\text{Mg}_{20}\text{Al}_{20}\text{Ti}_{20}\text{V}_{20}$ before and after PCT measurement at 250 °C.

machine learning [11,12], and using parameters such as VEC (valence electron concentration) and δ (atomic size mismatch) [13]. HEAs showed superior hydrogen storage property not only in a single phase alloy [14] but also in multi phases alloy [15]. Various types of HEAs have been developed with not only increased hydrogen storage capacity [8] but also enhanced activation properties [16], low temperature dehydrogenation property [15] and other desirable characteristics [17–19], such as cycling properties, gravimetric capacity of hydrogen, and catalytic effects for hydrogen storage materials.

In this study, the hydrogen absorption and desorption properties of Li-Mg-Al-Ti-M based lightweight HEAs, in which light metal elements, such as Li and Mg, are favorable for reducing the density, were investigated to improve their gravimetric capacity. This is because reducing the density of the alloy leads to an increase in the gravimetric capacity of hydrogen, even though H/M remains the same. Although the number of reported research about lightweight HEAs is limited, there is potential in lightweight HEAs to improve the gravimetric capacity of hydrogen [10]. Studying the research of lightweight HEAs with various compositions would be worth for development of hydrogen storage alloy with a high gravimetric capacity of hydrogen. Here, the Li-Mg-Al-Ti-M based lightweight HEAs were synthesized via mechanical alloying (MA) [20]. In a previous study, the equiatomic $\text{Li}_{20}\text{Mg}_{20}\text{Al}_{20}\text{Ti}_{20}\text{M}_{20}$ system was classified into four groups based on its crystal structure. The groups are as follows: (i) unmixed composites ($M = \text{Cr}, \text{Mn}, \text{Fe}$), (ii) intermetallic compounds ($M = \text{Ga}, \text{Ge}, \text{Sn}$), (iii) compounds with unidentifiable structures ($M = \text{Si}, \text{Co}, \text{Ni}, \text{Cu}, \text{Zn}, \text{Y}, \text{Zn}$), and (iv) solid solutions ($M = \text{V}, \text{Nb}$). Equiatomic $\text{Li}_{20}\text{Mg}_{20}\text{Al}_{20}\text{Ti}_{20}\text{V}_{20}$ and $\text{Li}_{20}\text{Mg}_{20}\text{Al}_{20}\text{Ti}_{20}\text{Nb}_{20}$ consist of Ti-V (or Ti-Nb) based BCC and Li-Mg based BCC phases. A single BCC phase was obtained in the Li-Mg-Al-Ti-V system by tuning its composition. Among the Li-Mg-Al-Ti-M based lightweight HEAs, a single BCC phases would be also obtained in the Li-Mg-Al-Ti-Nb lightweight HEAs. Thus, in this study, equiatomic $\text{Li}_{20}\text{Mg}_{20}\text{Al}_{20}\text{Ti}_{20}\text{V}_{20}$, single phases of Li-Mg-Al-Ti-V and Li-Mg-Al-Ti-Nb lightweight HEAs were selected to evaluate their hydrogen absorption and desorption properties.

2. Experimental procedures

$\text{Li}_{20}\text{Mg}_{20}\text{Al}_{20}\text{Ti}_{20}\text{V}_{20}$, $\text{Li}_8\text{Mg}_8\text{Al}_{28}\text{Ti}_{28}\text{V}_{28}$ and $\text{Li}_8\text{Mg}_8\text{Al}_{28}\text{Ti}_{28}\text{Nb}_{28}$ were synthesized using MA. The detailed sample preparation has been described in a previous study [20]. The MA was conducted using a planetary ball mill (FRITSCH P-7) with an SKD11 steel vessel and SUJ2 steel balls. Ball milling was conducted at a rotation speed of 400 rpm under 0.1 MPa Ar atmosphere. The ball-to-sample mass ratio was 96:1. The milling process was repeated 40 times, and the sample was milled for 20 h. Each process involved rotation for 30 min between 15 min

pauses to prevent excessive heating of the sample. All the sample preparations were performed under an Ar atmosphere (oxygen concentration less than 1 ppm) within a glove box (Miwa Manufacturing DBO-2LNKP-MM01) to reduce the effects of oxidation as much as possible.

Differential scanning calorimetry (DSC, RIGAKU DSC8230HP) was performed under 0.1 or 0.3 MPa H_2 atmosphere up to 400 °C with heating rate of 2 °C/min to determine the temperature for PCT (pressure composition temperature(isotherm)) measurement. Before the measurements, $\text{Li}_{20}\text{Mg}_{20}\text{Al}_{20}\text{Ti}_{20}\text{V}_{20}$ was activated at 1.0 MPa H_2 by heating up to 350 °C and cooling down to room temperature with a heating/cooling rate of 2 °C/min in the DSC equipment. PCT measurements were performed at room temperature and 250 °C by Sieverts-type equipment without any activation processes, including both pre hydrogenation/dehydrogenation and vacuuming under high temperatures. Hydrogen absorption kinetics of $\text{Li}_8\text{Mg}_8\text{Al}_{28}\text{Ti}_{28}\text{Nb}_{28}$ were examined under 2.0 MPa H_2 at room temperature using Sieverts-type equipment without any activation processes. After the hydrogen absorption kinetics measurement, the hydrogen desorption property of $\text{Li}_8\text{Mg}_8\text{Al}_{28}\text{Ti}_{28}\text{Nb}_{28}$ was evaluated by thermogravimetric and differential thermal analyses (TG-DTA, Bruker 2000SA) using a heating rate of 5 °C/min in He flow up to 500 °C in a glove box. The crystal structure of the phases in the samples was characterized by X-ray diffraction (XRD, Rigaku SmartLab (Cu $K_{\alpha 1}$) and RINT-2500V (Cu $K_{\alpha 2}$)). The XRD measurements were performed without exposing the samples to air by covering them with a polyimide film. Scanning transmission electron microscope (STEM, FEI Titan3 G2 60–300) observation was conducted to evaluate the microstructures without exposing the samples to air by using non atmosphere exposed STEM holder. The STEM samples were fabricated to thin film from powder using focused ion beam (FIB). The pickup process was performed by FIB (Hitachi High-Tech FB-2100) and the thinning process was performed by FIB- scanning electron microscopy (FIB-SEM, JEOL JIB-4600F/HKD). Both FIB fabrications were conducted without exposing the samples to air by using non atmosphere exposed holder. The sample transfer of holder to holder was conducted in the glove box, so the samples were not exposed to air.

3. Results and discussion

3.1. Hydrogen absorption and desorption property of equiatomic $\text{Li}_{20}\text{Mg}_{20}\text{Al}_{20}\text{Ti}_{20}\text{V}_{20}$

XRD measurements were performed to confirm the crystal structures of the phases formed in the synthesized alloy. The top row of Fig. 1 shows the XRD pattern of equiatomic $\text{Li}_{20}\text{Mg}_{20}\text{Al}_{20}\text{Ti}_{20}\text{V}_{20}$ synthesized by MA. Diffraction peaks corresponding to the BCC phase and an additional peak are observed. The lattice constant of the main BCC phase was $a = 3.175 \text{ \AA}$, which is almost same as that of equiatomic Ti-V solid solution at $a = 3.165 \text{ \AA}$ [21]. Hence, the main BCC phase (labeled with circles) was assigned as a Ti-V based BCC solid solution. However, an additional peak located at approximately 36 °, which was not identified as the Ti-V phase, was also observed in Fig. 1. Assuming that this peak corresponds to a BCC phase, its lattice constant was calculated to be $a = 3.522 \text{ \AA}$. This is close to that of equiatomic LiMg solid solution at $a = 3.484 \text{ \AA}$ [22]. Because Li and Mg are immiscible with Ti and V in the equilibrium state, the small peak (labeled with a star) was probably a Li-Mg based BCC solid solution that did not dissolve into the Ti-V phase. Because the lattice constant of the Li-Mg based solid solution was smaller than that of equiatomic LiMg solid solution, the composition of the Li-Mg base solid solution might not be equiatomic, or some elements might be dissolved into the Li-Mg phase. We could not distinguish between the Ti-V and Li-Mg based phases using conventional SEM-energy dispersive spectroscopy (EDS) observations in previous study [20]. Considering SEM-EDS result and broad peaks in the XRD, Ti-V based phase and Li-Mg based phase would be fine distributed. For equiatomic $\text{Li}_{20}\text{Mg}_{20}\text{Al}_{20}\text{Ti}_{20}\text{V}_{20}$, it was shown that two BCC phases, which were

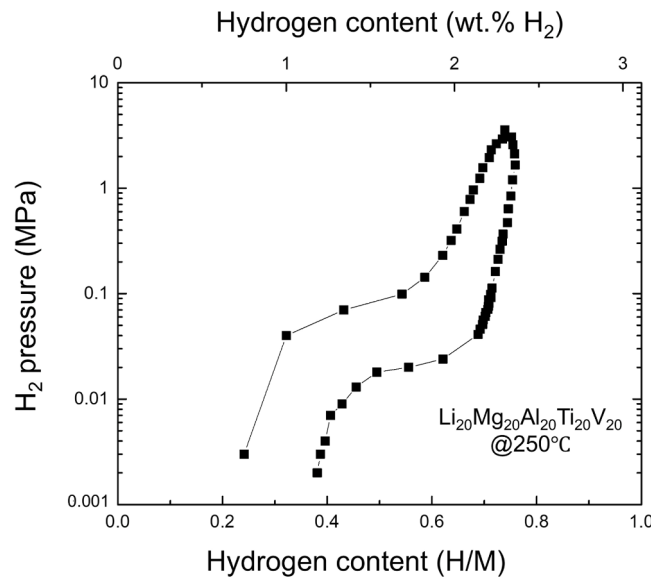


Fig. 2. PCT curve of $\text{Li}_{20}\text{Mg}_{20}\text{Al}_{20}\text{Ti}_{20}\text{V}_{20}$ at 250 °C.

Ti-V based, and Li-Mg based solid solutions, were synthesized by MA, similar to a previous study [20].

Next, the hydrogen absorption and desorption properties of equiatomic $\text{Li}_{20}\text{Mg}_{20}\text{Al}_{20}\text{Ti}_{20}\text{V}_{20}$ were investigated using DSC and PCT measurements. The DSC experiment, which was performed in 0.1 MPa H_2 atmosphere from room temperature to 500 °C after activated, indicated that equiatomic $\text{Li}_{20}\text{Mg}_{20}\text{Al}_{20}\text{Ti}_{20}\text{V}_{20}$ absorbs and desorbs hydrogen at approximately 250 °C (Figure S1, in supplementary material). Fig. 2 shows the PCT curve of equiatomic $\text{Li}_{20}\text{Mg}_{20}\text{Al}_{20}\text{Ti}_{20}\text{V}_{20}$ measured at 250 °C. Regarding the absorption process, a plateau region was observed at 0.04–0.10 MPa, and the plateau range was $\text{H}/\text{M} = 0.37$. The maximum hydrogen absorption of $\text{Li}_{20}\text{Mg}_{20}\text{Al}_{20}\text{Ti}_{20}\text{V}_{20}$ reached $\text{H}/\text{M} = 0.74$, which corresponds to 2.3 wt% H_2 . On the other hand, in the desorbing process, a plateau region was observed at 0.02–0.03 MPa, and the plateau range was $\text{H}/\text{M} = 0.23$. The H/M after PCT was approximately 0.4. Regarding to the hydrogen desorption of $\text{Li}_{20}\text{Mg}_{20}\text{Al}_{20}\text{Ti}_{20}\text{V}_{20}$, the plateau pressure of equiatomic $\text{Li}_{20}\text{Mg}_{20}\text{Al}_{20}\text{Ti}_{20}\text{V}_{20}$ was almost comparable to that of ball-milled pure Mg [23]. As shown in Fig. 1, a Mg phase with a hexagonal close-packed (HCP) appeared, and

the Li-Mg BCC phase disappeared in the XRD pattern after the PCT measurement, although no significant changes were observed in the peaks of Ti-V phase. These suggest that Mg would separate from the Li-Mg phase during the hydrogen absorption and desorption processes. This is consistent with a previous report that MgH_2 formed in the AZ31 alloy with 15 wt% Li, which consists of the BCC phase, due to hydrogen absorption [24]. Thus, the plateau pressure of the absorption process would be attributed to the formation of MgH_2 from the Li-Mg phase. Assuming that all Mg in $\text{Li}_{20}\text{Mg}_{20}\text{Al}_{20}\text{Ti}_{20}\text{V}_{20}$ forms MgH_2 , the hydrogen absorption amount of $\text{Li}_{20}\text{Mg}_{20}\text{Al}_{20}\text{Ti}_{20}\text{V}_{20}$ should be $\text{H}/\text{M} = 0.4$. This H/M value is slightly larger than that of plateau region of the absorption process ($\text{H}/\text{M} = 0.37$). Therefore, most of the Mg in $\text{Li}_{20}\text{Mg}_{20}\text{Al}_{20}\text{Ti}_{20}\text{V}_{20}$ could form MgH_2 in the hydrogen absorption process.

Herein, the crystal structure of $\text{Li}_{20}\text{Mg}_{20}\text{Al}_{20}\text{Ti}_{20}\text{V}_{20}$ and the lattice constants of the phases observed before and after PCT measurements are discussed. While the XRD profile before the PCT measurement showed two BCC phases with Ti-V and Li-Mg based phases in $\text{Li}_{20}\text{Mg}_{20}\text{Al}_{20}\text{Ti}_{20}\text{V}_{20}$, Ti-V based BCC and Mg HCP phases were identified after the PCT measurement. The lattice constant of the Mg HCP phase in $\text{Li}_{20}\text{Mg}_{20}\text{Al}_{20}\text{Ti}_{20}\text{V}_{20}$ and that of pure Mg were $a = 3.209 \text{ \AA}$, $c = 5.211 \text{ \AA}$ and $a = 3.214 \text{ \AA}$, $c = 5.219 \text{ \AA}$, respectively. Because the atomic radius of Li (152 pm) is smaller than that of Mg (160 pm), a part of Li might be solved in Mg phase. However, equiatomic LiMg phase is BCC, all Li in the Li-Mg phase were not solved into the Mg phase. Considering the disappearance of the Li-Mg phase and the appearance of the Mg phase by hydrogen absorption and desorption processes, the phase separation of Li from the Li-Mg phase could occur as well as Mg. In contrast, the Ti-V base BCC phase was identified both before and after the PCT measurement. The lattice constants for these were $a = 3.175 \text{ \AA}$ and $a = 3.204 \text{ \AA}$, respectively. This small expansion of the lattice constant of Ti-V based BCC after the PCT measurement would be due to the remaining hydrogen solute. If the expansion of the lattice constant of Ti-V based BCC is entirely due to hydrogen occupation, the amount of hydrogen is $\text{H}/\text{M} = 0.14\text{--}0.23$. This H/M was calculated from that the volume expansion is $2.9 \pm 0.3 \text{ \AA}^3$ per hydrogen atom in the T-site of d-band metals and $2.2 \pm 0.3 \text{ \AA}^3$ per hydrogen atom in the O-site of d-band metals [25]. The $\text{H}/\text{M} = 0.14\text{--}0.23$ calculated from the lattice volume expansion was not consistent with the remaining hydrogen in $\text{Li}_{20}\text{Mg}_{20}\text{Al}_{20}\text{Ti}_{20}\text{V}_{20}$ after the PCT measurement, which is $\text{H}/\text{M} = 0.38$. If Li in $\text{Li}_{20}\text{Mg}_{20}\text{Al}_{20}\text{Ti}_{20}\text{V}_{20}$ forms LiH upon hydrogen absorption, the hydrogen in LiH remains even after the PCT measurement at 250 °C because LiH requires high temperature for hydrogen desorption, such as 710 °C in

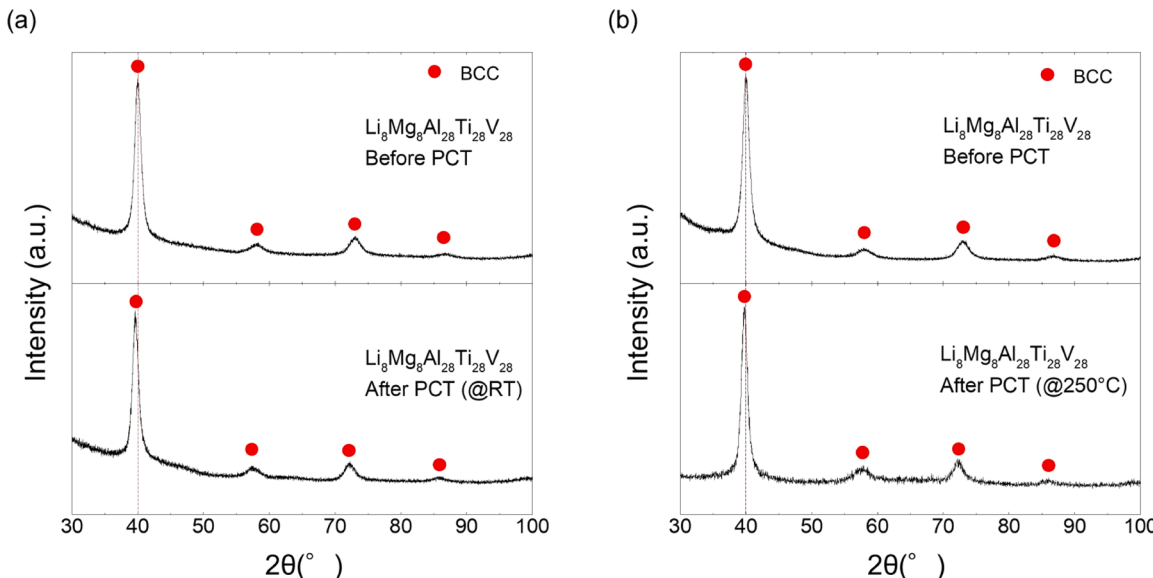


Fig. 3. XRD patterns of $\text{Li}_8\text{Mg}_8\text{Al}_{28}\text{Ti}_{28}\text{V}_{28}$ before and after PCT measurement (a) at room temperature (b) at 250 °C.

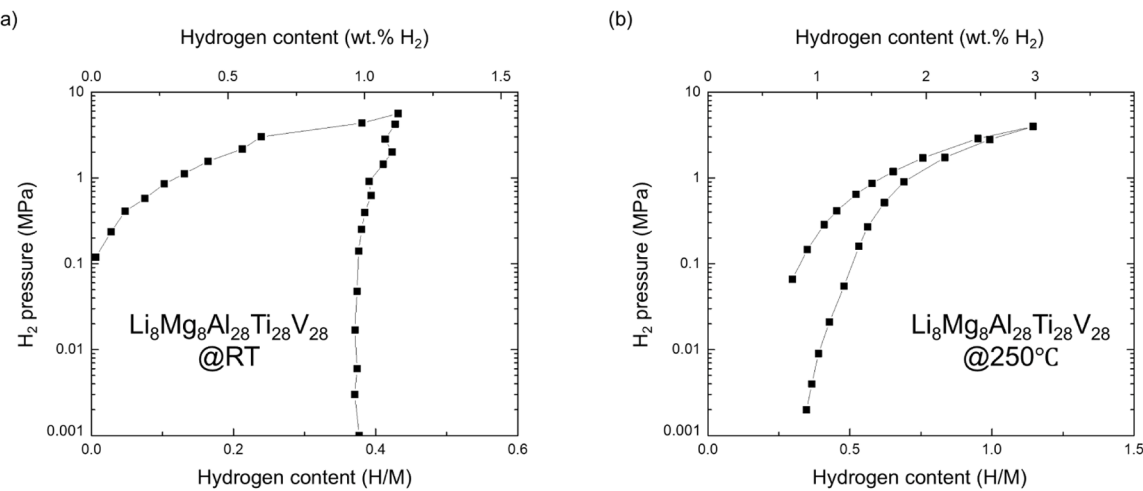


Fig. 4. Initial PCT curves of $\text{Li}_8\text{Mg}_8\text{Al}_{28}\text{Ti}_{28}\text{V}_{28}$ (a) at room temperature (b) at 250 °C.

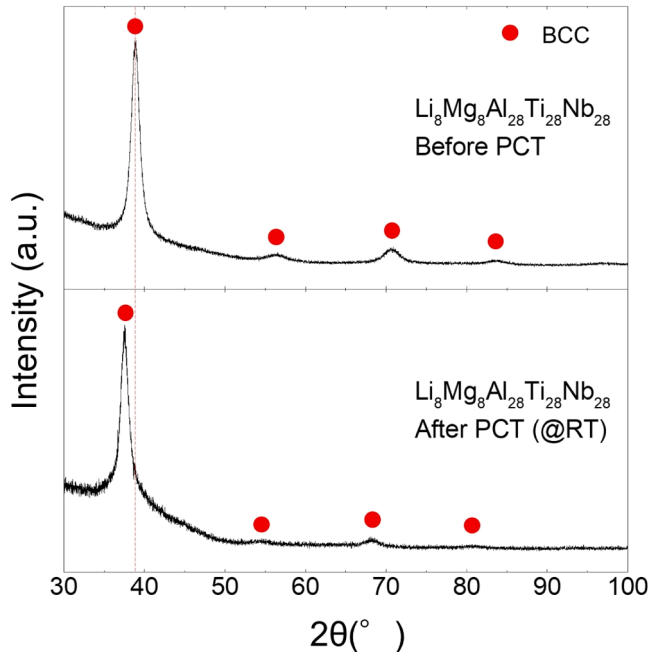


Fig. 5. XRD patterns before and after PCT measurement of $\text{Li}_8\text{Mg}_8\text{Al}_{28}\text{Ti}_{28}\text{Nb}_{28}$ at room temperature.

5×10^{-3} MPa [26]. In this case, the sum of the hydrogen amount of LiH ($\text{H}/\text{M} \leq 0.2$) and that calculated from the lattice volume expansion of the Ti-V based BCC phase ($\text{H}/\text{M} = 0.14\text{--}0.23$) is almost equivalent to the remaining $\text{H}/\text{M} = 0.38$. Therefore, the Li in $\text{Li}_{20}\text{Mg}_{20}\text{Al}_{20}\text{Ti}_{20}\text{V}_{20}$ may form independent LiH upon hydrogen absorption. This hypothesis does not contradict with that Mg forms MgH_2 following formation of LiH at hydrogen absorption process in Li-Mg alloy which consists of BCC phase [27]. $\text{Li}_{20}\text{Mg}_{20}\text{Al}_{20}\text{Ti}_{20}\text{V}_{20}$ would absorb hydrogen through the hydrogen solution into the Ti-V based BCC phase and the formation of MgH_2 and LiH from the Li-Mg based BCC phase.

Although $\text{Li}_{20}\text{Mg}_{20}\text{Al}_{20}\text{Ti}_{20}\text{V}_{20}$ absorbed and desorbed hydrogen, applying $\text{Li}_{20}\text{Mg}_{20}\text{Al}_{20}\text{Ti}_{20}\text{V}_{20}$ to hydrogen storage alloys was challenging. One of these challenges was the phase separation caused by hydrogen absorption and desorption; the Li-Mg based BCC phase disappeared and the Mg HCP phase appeared, resulting in an irreversible reaction. However, no clear phase separation was observed in the Ti-V based BCC phase in $\text{Li}_{20}\text{Mg}_{20}\text{Al}_{20}\text{Ti}_{20}\text{V}_{20}$, even after hydrogen

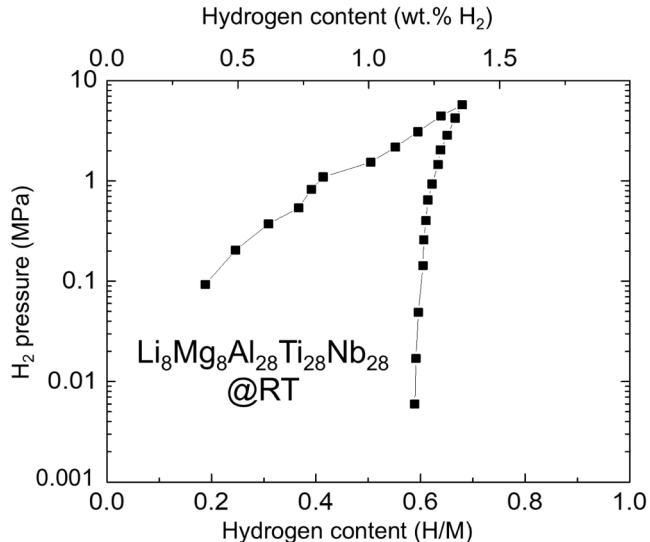


Fig. 6. Initial PCT curve of $\text{Li}_8\text{Mg}_8\text{Al}_{28}\text{Ti}_{28}\text{Nb}_{28}$ at room temperature.

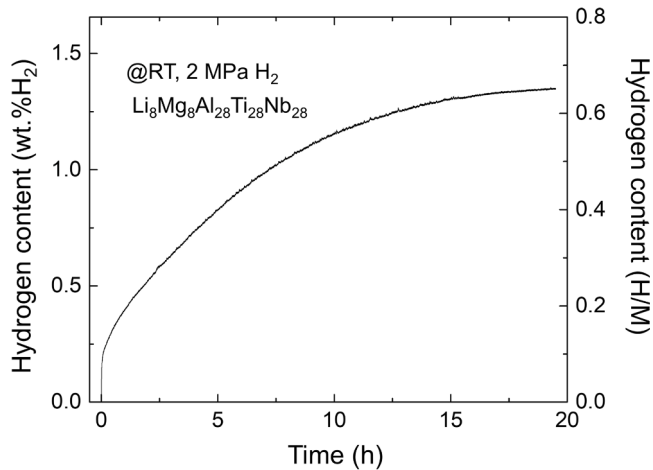


Fig. 7. Hydrogen absorption curve of $\text{Li}_8\text{Mg}_8\text{Al}_{28}\text{Ti}_{28}\text{Nb}_{28}$ under 2 MPa H₂ at room temperature.

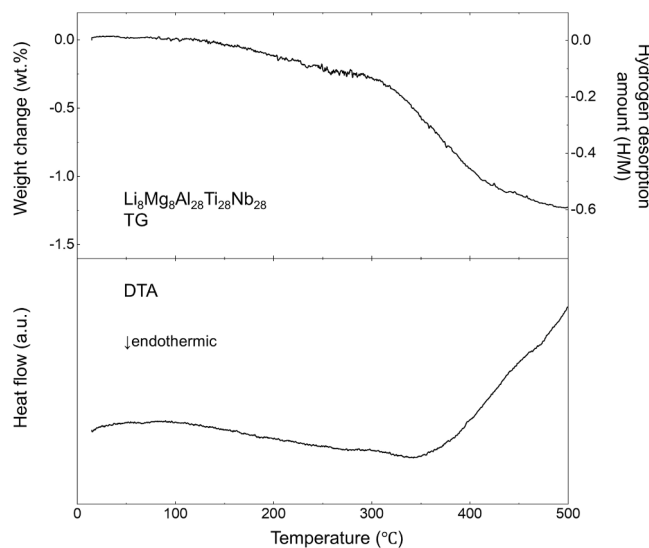


Fig. 8. Hydrogen desorption property of $\text{Li}_8\text{Mg}_8\text{Al}_{28}\text{Ti}_{28}\text{Nb}_{28}$ by TG-DTA.

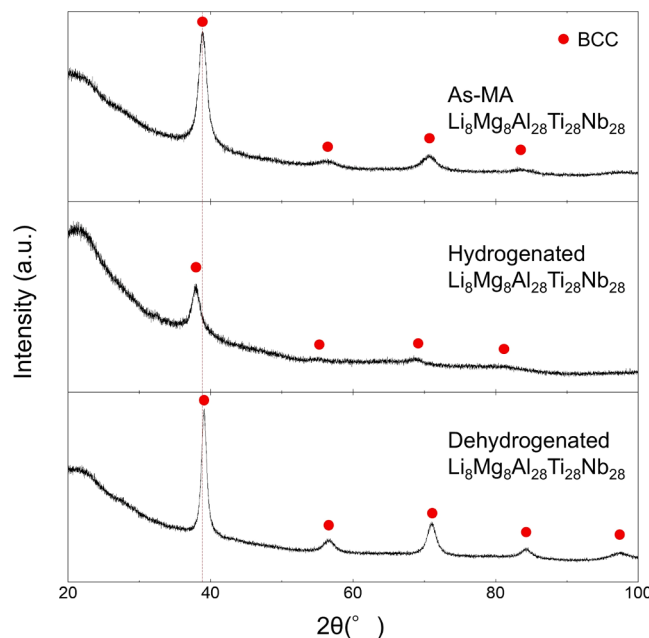


Fig. 9. XRD patterns of $\text{Li}_8\text{Mg}_8\text{Al}_{28}\text{Ti}_{28}\text{Nb}_{28}$ before and after hydrogenated/dehydrogenated. Hydrogenated state is after hydrogen absorption kinetics test (Fig. 7). Dehydrogenated state is after TG-DTA measurement (Fig. 8).

absorption and desorption, as shown by the XRD spectra. Therefore, we focused on lightweight HEAs with Ti-V based BCC single phase to suppress phase separation.

3.2. Hydrogen absorption and desorption property of single BCC phase $\text{Li}_8\text{Mg}_8\text{Al}_{28}\text{Ti}_{28}\text{V}_{28}$

The hydrogen absorption and desorption properties of a single Ti-V based BCC phase were investigated to suppress the phase separation. $\text{Li}_8\text{Mg}_8\text{Al}_{28}\text{Ti}_{28}\text{V}_{28}$, consisting of a single BCC phase, was synthesized by MA, same as previous study [20] as shown in the top row of Fig. 3. Only the peaks from the BCC phase were observed in the XRD pattern. Because the lattice constant was close to that of the Ti-V based BCC phase in $\text{Li}_{20}\text{Mg}_{20}\text{Al}_{20}\text{Ti}_{20}\text{V}_{20}$, the peaks (labeled with circles) were assigned to a BCC structure corresponding to the Ti-V based solid

solution. The lattice constants of the BCC phase in the top row of Fig. 3(a) and (b) are $a = 3.177 \text{ \AA}$ and 3.175 \AA , respectively. Because the sample was synthesized by MA, these lattice constants differed slightly from batch to batch. This lattice constant difference is negligible in terms of the hydrogen absorption and desorption properties. Although the Li-Mg phase was formed in equiatomic $\text{Li}_{20}\text{Mg}_{20}\text{Al}_{20}\text{Ti}_{20}\text{V}_{20}$, it was not observed in $\text{Li}_8\text{Mg}_8\text{Al}_{28}\text{Ti}_{28}\text{V}_{28}$. This suggests the presence of smaller amounts of Li and Mg solutes in the Ti-V based BCC phase of $\text{Li}_8\text{Mg}_8\text{Al}_{28}\text{Ti}_{28}\text{V}_{28}$.

Next, the hydrogen absorption and desorption properties of $\text{Li}_8\text{Mg}_8\text{Al}_{28}\text{Ti}_{28}\text{V}_{28}$ with a single BCC phase were investigated using DSC and PCT measurements. The DSC experiment, which was performed in a 0.3 MPa H_2 atmosphere from room temperature to 500°C , indicated that $\text{Li}_8\text{Mg}_8\text{Al}_{28}\text{Ti}_{28}\text{V}_{28}$ absorbed hydrogen close to room temperature (Figure S2, in Supplementary material). Fig. 4(a) shows the PCT curve of $\text{Li}_8\text{Mg}_8\text{Al}_{28}\text{Ti}_{28}\text{V}_{28}$ measured at room temperature. Similar to the DSC data, the PCT curve showed that $\text{Li}_8\text{Mg}_8\text{Al}_{28}\text{Ti}_{28}\text{V}_{28}$ absorbed hydrogen at room temperature in the amount of $\text{H}/\text{M} = 0.43$, which corresponds to 1.1 wt\% H_2 . In the PCT curve, no clear plateau region is observed, and almost no hydrogen is desorbed at room temperature. XRD measurement was performed after the PCT measurement to investigate the effect of hydrogen absorption on the phase stability. As shown in Fig. 3(a), only the BCC phase was observed in $\text{Li}_8\text{Mg}_8\text{Al}_{28}\text{Ti}_{28}\text{V}_{28}$ after the PCT measurement. The XRD results suggested that no clear phase separation occurred in $\text{Li}_8\text{Mg}_8\text{Al}_{28}\text{Ti}_{28}\text{V}_{28}$ after hydrogen absorption. The diffraction peaks of the BCC phase shifted to the lower 2θ angle side compared with that before PCT measurement. The estimated lattice constant of the BCC phase after the PCT measurement was $a = 3.204 \text{ \AA}$, which was slightly larger than that before PCT. This lattice expansion would be due to the hydrogen absorption. Based on the XRD results and PCT curve, the BCC phase of $\text{Li}_8\text{Mg}_8\text{Al}_{28}\text{Ti}_{28}\text{V}_{28}$ could absorb hydrogen in the solid solute state at room temperature.

Because phase separation was not observed in $\text{Li}_8\text{Mg}_8\text{Al}_{28}\text{Ti}_{28}\text{V}_{28}$ upon hydrogenation at room temperature, PCT measurements were performed at 250°C . As shown in Fig. 4(b), the maximum H/M reached 1.14 , which corresponds to 3.0 wt\% H_2 . In the PCT curve, no clear plateau region was observed at 250°C . On the other hand, hydrogen desorption was observed at 250°C . The amount of hydrogen desorbed was $\text{H}/\text{M} = 0.80$, which corresponds to 2.1 wt\% H_2 at 250°C . XRD was performed on $\text{Li}_8\text{Mg}_8\text{Al}_{28}\text{Ti}_{28}\text{V}_{28}$ after the PCT measurements to investigate the effects of hydrogen absorption and desorption on the phase transformation. As shown in Fig. 3(b), only the BCC phase was observed in $\text{Li}_8\text{Mg}_8\text{Al}_{28}\text{Ti}_{28}\text{V}_{28}$ after the PCT measurement. The peak of the BCC phase shifted to the lower 2θ angle side compared with that before the PCT measurement, and the lattice constant of the BCC phase after the PCT measurement was $a = 3.196 \text{ \AA}$ which is smaller than that after PCT measurement at room temperature. This must come from the different residual hydrogen amounts. PCT and XRD results indicated that $\text{Li}_8\text{Mg}_8\text{Al}_{28}\text{Ti}_{28}\text{V}_{28}$ could absorb and desorb hydrogen without clear phase separation.

3.3. Hydrogen absorption and desorption property of single BCC phase $\text{Li}_8\text{Mg}_8\text{Al}_{28}\text{Ti}_{28}\text{Nb}_{28}$

Although $\text{Li}_8\text{Mg}_8\text{Al}_{28}\text{Ti}_{28}\text{V}_{28}$ absorbed hydrogen at room temperature, the hydrogen absorption amount was not so much. Therefore, V was changed to Nb as a constituent of the lightweight HEAs to improve hydrogen absorption. Because Nb has a higher affinity for hydrogen than V, the lightweight HEAs, including Nb might have a larger hydrogen absorption H/M than V, even though Nb has a higher density. $\text{Li}_8\text{Mg}_8\text{Al}_{28}\text{Ti}_{28}\text{Nb}_{28}$ was synthesized by MA, and the top row of Fig. 5 shows the XRD pattern. Only the diffraction peaks corresponding to the BCC phase were observed. The peaks (labeled with circles) were assigned as a Ti-Nb based BCC solid solution, and the lattice constant was $a = 3.271 \text{ \AA}$. A single BCC phase was synthesized in the Li-Mg-Al-Ti-Nb system, similar to the Li-Mg-Al-Ti-V system. The lattice constant of

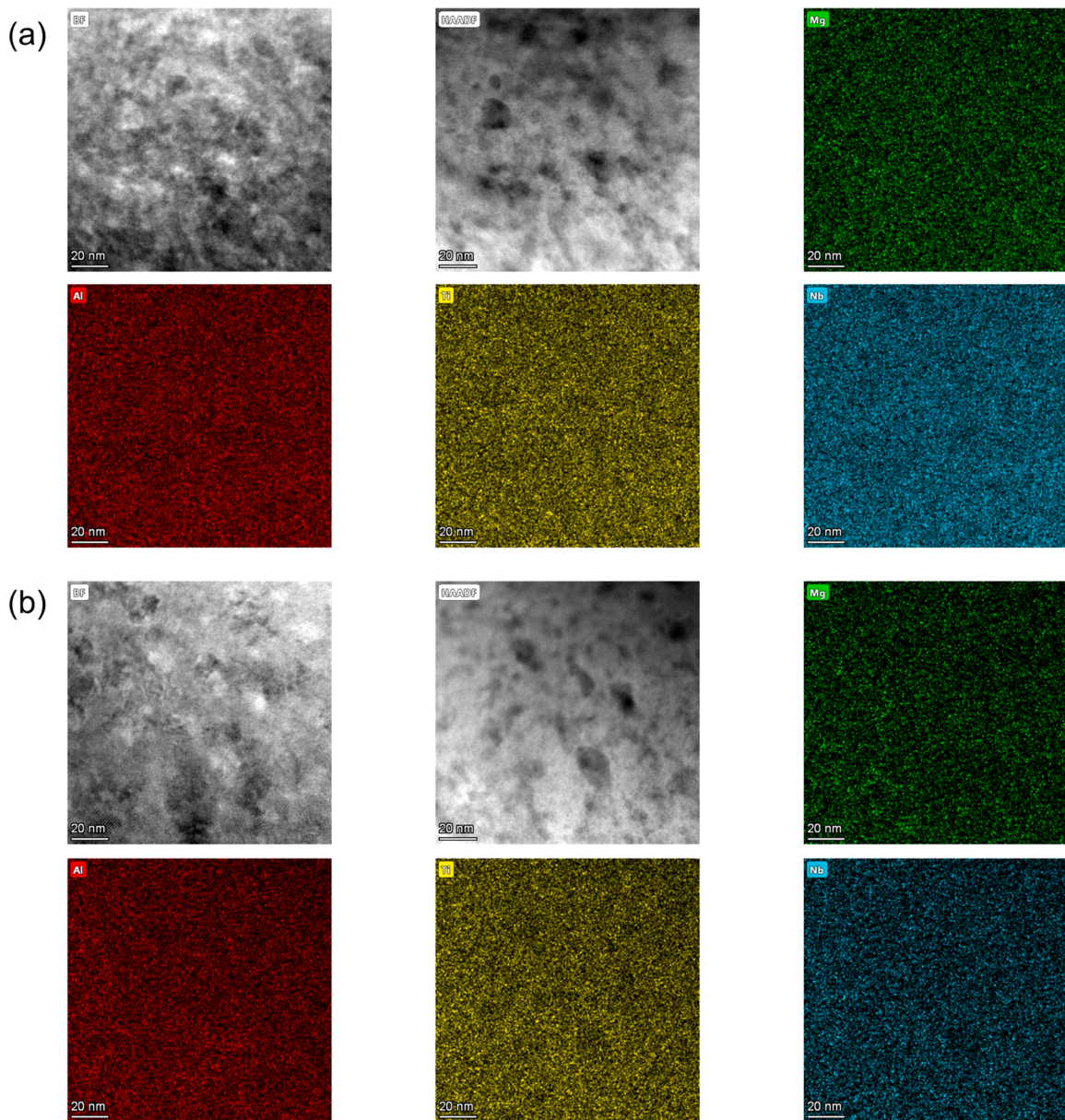


Fig. 10. STEM-EDS images of $\text{Li}_8\text{Mg}_8\text{Al}_{28}\text{Ti}_{28}\text{Nb}_{28}$ (a) before hydrogenated (as-MA) (b) after hydrogenated.

$\text{Li}_8\text{Mg}_8\text{Al}_{28}\text{Ti}_{28}\text{Nb}_{28}$ is larger than that of $\text{Li}_8\text{Mg}_8\text{Al}_{28}\text{Ti}_{28}\text{V}_{28}$ because the atomic radius of Nb (143 pm) is larger than that of V (132 pm).

Next, the hydrogen absorption and desorption properties of $\text{Li}_8\text{Mg}_8\text{Al}_{28}\text{Ti}_{28}\text{Nb}_{28}$ with a single BCC phase were investigated using DSC and PCT measurements. The DSC experiment, which was performed in a 0.3 MPa H_2 atmosphere from room temperature to 500 °C, indicated that $\text{Li}_8\text{Mg}_8\text{Al}_{28}\text{Ti}_{28}\text{Nb}_{28}$ could absorb hydrogen close to room temperature (Figure S3, in supplementary material). Fig. 6 shows the PCT curve of $\text{Li}_8\text{Mg}_8\text{Al}_{28}\text{Ti}_{28}\text{Nb}_{28}$ measured at room temperature. The amount of absorbed hydrogen at room temperature was $\text{H}/\text{M} = 0.68$, which corresponds to 1.4 wt% H_2 . In the PCT curve, no clear plateau region is observed, and almost no hydrogen is desorbed at room temperature. As shown in Fig. 5, only the BCC phase was observed in $\text{Li}_8\text{Mg}_8\text{Al}_{28}\text{Ti}_{28}\text{Nb}_{28}$ after the PCT measurement. In other words, no clear phase separation was observed in the XRD pattern of $\text{Li}_8\text{Mg}_8\text{Al}_{28}\text{Ti}_{28}\text{Nb}_{28}$ after hydrogen absorption. The peaks of the BCC phase shifted to the lower 20 angle side compared to that before the PCT measurement. The lattice constant of the BCC phase after the PCT measurement was $a = 3.348 \text{ \AA}$. The lattice constant would expand due to hydrogen absorption.

The hydrogen absorption kinetics at room temperature and hydrogen desorption upon heating of $\text{Li}_8\text{Mg}_8\text{Al}_{28}\text{Ti}_{28}\text{Nb}_{28}$ were examined, because the hydrogen absorption amount of $\text{Li}_8\text{Mg}_8\text{Al}_{28}\text{Ti}_{28}\text{Nb}_{28}$ was larger than that of $\text{Li}_8\text{Mg}_8\text{Al}_{28}\text{V}_{28}$ at room temperature. First, the hydrogen absorption kinetics of $\text{Li}_8\text{Mg}_8\text{Al}_{28}\text{Ti}_{28}\text{Nb}_{28}$ were examined under 2.0 MPa H_2 at room temperature, as shown in Fig. 7. The alloy absorbed hydrogen up to $\text{H}/\text{M} = 0.65$. The amount of hydrogen absorbed in the hydrogen absorption kinetics test was comparable to that observed in the PCT measurements. In the absorption curve, no obvious incubation period was observed though this was the first cycle of hydrogen absorption/desorption without any activation processes. Because the alloys synthesized by MA had already activated the surface, no obvious incubation period would be observed. The alloy required more than ten hours to saturate hydrogen absorption. The hydrogen absorption kinetics of $\text{Li}_8\text{Mg}_8\text{Al}_{28}\text{Ti}_{28}\text{Nb}_{28}$ were relatively slower than those of previously reported Li-containing lightweight HEAs [28].

The hydrogen desorption properties of $\text{Li}_8\text{Mg}_8\text{Al}_{28}\text{Ti}_{28}\text{Nb}_{28}$ were examined using TG-DTA. Because $\text{Li}_8\text{Mg}_8\text{Al}_{28}\text{Ti}_{28}\text{Nb}_{28}$ desorbed almost no hydrogen at room temperature, TG-DTA was performed to

investigate its hydrogen desorption properties. Fig. 8 shows the TG-DTA results. It indicates that the alloy desorbed hydrogen at H/M = 0.59 (1.2 wt% H₂) up to 500 °C as an endothermic reaction. The hydrogen absorption amount was almost consistent with the hydrogen desorption amount in the TG, thereby Li₈Mg₈Al₂₈Ti₂₈Nb₂₈ would desorb almost all hydrogen up to 500 °C. The hydrogen desorption temperature of Li₈Mg₈Al₂₈Ti₂₈Nb₂₈ would be almost comparable to that of currently reported lightweight HEAs. The range of main hydrogen desorption temperatures of lightweight HEAs is 200–400 °C for most alloys, as previously reported [28–35]. As shown in Fig. 9, the XRD results showed that only the BCC phase was observed in all states of Li₈Mg₈Al₂₈Ti₂₈Nb₂₈: as-MA, after hydrogen absorption, and after hydrogen desorption. The lattice constant of the as-MA, the hydrogenated and dehydrogenated states were $a = 3.266, 3.341$, and 3.254 \AA , respectively. These results indicate that Li₈Mg₈Al₂₈Ti₂₈Nb₂₈ could absorb and desorb hydrogen without clear phase separation, because new phases were not observed even after hydrogen absorption and desorption. Interestingly the lattice constant of the dehydrogenated Li₈Mg₈Al₂₈Ti₂₈Nb₂₈ was smaller than that of as-MA. This difference in the lattice constants cannot be explained by considering only the shrinkage of the lattice constants owing to hydrogen desorption. One of the possible reasons for this could be the compositional change of the metal elements upon local microscopic segregation.

The microstructures of Li₈Mg₈Al₂₈Ti₂₈Nb₂₈ before and after hydrogenated were evaluated using STEM-EDS and the images are shown in Fig. 10. Constituent elements, except for Li which cannot be detected conventional EDS, are distributed almost uniform both before (Fig. 10 (a)) and after hydrogenation (Fig. 10 (b)). There were no significant differences between the microstructures before and after hydrogenation based on Bright Field (BF) and High Angle Annular Dark Field (HAADF) images. These results are consistent with the other experimental results, which show that Li₈Mg₈Al₂₈Ti₂₈Nb₂₈ absorbs hydrogen without clear phase separation.

The hydrogen absorption amounts of Li₈Mg₈Al₂₈Ti₂₈V₂₈ and Li₈Mg₈Al₂₈Ti₂₈Nb₂₈ were H/M = 0.43–1.14 and did not reach that of TiVZrNbHf (H/M = 2.5) [8]. One possible reason why the lightweight HEAs in this study does not exhibit such a high hydrogen storage capacity may be the high Al content in alloys composition. It has been reported in literature that hydrogen absorption decreases with increasing Al content in BCC alloys [36–38]. Therefore, tuning the chemical composition may be effective for improving the amount of hydrogen absorbed. However, the gravimetric hydrogen capacity of the alloys (1.1–3.0 wt% H₂) were not far from that of TiVZrNbHf (2.7 wt% H₂) [8] due to the low density of these alloys. The calculated densities of for the Li₈Mg₈Al₂₈Ti₂₈V₂₈, Li₈Mg₈Al₂₈Ti₂₈Nb₂₈, and TiVZrNbHf alloys were 3.7, 4.5, 8.9 g/cm³, respectively. If the H/M of these alloys can be improved to 2, the gravimetric hydrogen capacity could exceed 5 wt% H₂ due to the low density of these alloys. Furthermore, these alloys can absorb hydrogen at room temperature without activation process. Although there are several challenges currently, such as low H/M and high desorption temperature, this study showed that lightweight HEAs are worth researching for hydrogen storage alloy. The ultimate goal of our research is to apply lightweight HEAs to hydrogen tanks in fuel cell vehicles, so the hydrogen absorption and desorption properties of the lightweight HEAs should be improved in the future work.

4. Conclusion

In this study, the applicability of Li-Mg-Al-Ti-V and Li-Mg-Al-Ti-Nb based lightweight HEAs as hydrogen-storage alloys was investigated. The hydrogen absorption and desorption properties of Li₂₀Mg₂₀Al₂₀Ti₂₀V₂₀, Li₈Mg₈Al₂₈Ti₂₈V₂₈ and Li₈Mg₈Al₂₈Ti₂₈Nb₂₈ were presented. Equiatomic Li₂₀Mg₂₀Al₂₀Ti₂₀V₂₀ consisted of two phases; Ti-V based BCC phase and Li-Mg based BCC phase. Li₂₀Mg₂₀Al₂₀Ti₂₀V₂₀ absorbed hydrogen up to H/M = 0.74 (2.3 wt% H₂) at 250 °C. In this absorption process, MgH₂ and LiH formed from the Li-Mg BCC phase. This

precipitated Mg phase mainly contributed to reversible hydrogenation reaction. Li₈Mg₈Al₂₈Ti₂₈V₂₈ and Li₈Mg₈Al₂₈Ti₂₈Nb₂₈ consisted of a single BCC phase that absorbed hydrogen at H/M = 0.43 (1.1 wt% H₂) and H/M = 0.68 (1.4 wt% H₂), respectively, at room temperature without clear phase separation. Furthermore, Li₈Mg₈Al₂₈Ti₂₈Nb₂₈ desorbed almost all hydrogen up to 500 °C without clear phase separation. Although the gravimetric hydrogen capacities of studied Li₈Mg₈Al₂₈Ti₂₈V₂₈ and Li₈Mg₈Al₂₈Ti₂₈Nb₂₈ are not sufficiently large, lightweight HEAs would have the potential for their application in fuel cell vehicle tanks.

CRediT authorship contribution statement

Hirotada Hashimoto: Conceptualization, Funding acquisition, Investigation, Visualization, Writing – original draft, **Shigehito Isobe:** Conceptualization, Funding acquisition, Project administration, Supervision, Writing – review and editing, **Tatsuya Minami:** Conceptualization, Investigation, Visualization, **Kohta Asano:** Investigation, Writing – review and editing, **Kouji Sakaki:** Investigation, Writing – review and editing, **Naoyuki Hashimoto:** Writing – review and editing, **Hiroshi Oka:** Writing – review and editing

Declaration of Competing Interest

The authors declare that they have no known competing financial interests or personal relationships that could have appeared to influence the work reported in this paper.

Acknowledgements

This work was partially supported by a JSPS Grant-in-Aid for Scientific Research JP21H00137, JST SPRING Grant Number JPMJSP2119, and The Light Metal Educational Foundation, Inc.

Supplementary data associated with this article can be found in the online version at doi:10.1016/j.nxmate.2025.101067.

Appendix A. Supporting information

Supplementary data associated with this article can be found in the online version at doi:10.1016/j.nxmate.2025.101067.

References

- [1] L. Schlapbach, A. Züttel, Hydrogen-storage materials for mobile applications, *Nature* 414 (2001) 353–358, <https://doi.org/10.1038/35104634>.
- [2] A. Züttel, Materials for hydrogen storage, *Mater. Today* 6 (2003) 24–33, [https://doi.org/10.1016/S1369-7021\(03\)00922-2](https://doi.org/10.1016/S1369-7021(03)00922-2).
- [3] I.P. Jain, C. Lal, A. Jain, Hydrogen storage in mg: a most promising material, *Int. J. Hydrol. Energy* 35 (2010) 5133–5144, <https://doi.org/10.1016/j.ijhydene.2009.08.088>.
- [4] C. Liu, Z. Yuan, X. Li, Y. Sun, T. Zhai, Z. Han, et al., Review on improved hydrogen storage properties of MgH₂ by adding new catalyst, *J. Energy Storage* 97 (2024), <https://doi.org/10.1016/j.est.2024.112786>.
- [5] J.W. Yeh, Alloy design strategies and future trends in high-entropy alloys, *JOM* 65 (2013) 1759–1771, <https://doi.org/10.1007/s11837-013-0761-6>.
- [6] D.B. Miracle, O.N. Senkov, A critical review of high entropy alloys and related concepts, *Acta Mater.* 122 (2017) 448–511, <https://doi.org/10.1016/j.actamat.2016.08.081>.
- [7] M.H. Tsai, J.W. Yeh, High-entropy alloys: a critical review, *Mater. Res. Lett.* 2 (2014) 107–123, <https://doi.org/10.1080/21663831.2014.912690>.
- [8] M. Sahlberg, D. Karlsson, C. Zlotea, U. Jansson, Superior hydrogen storage in high entropy alloys, *Sci. Rep.* 6 (2016), <https://doi.org/10.1038/srep36770>.
- [9] M.M. Nygård, G. Ek, D. Karlsson, M. Sahlberg, M.H. Sorby, B.C. Hauback, Hydrogen storage in high-entropy alloys with varying degree of local lattice strain, *Int. J. Hydrol. Energy* 44 (2019) 29140–29149, <https://doi.org/10.1016/j.ijhydene.2019.03.223>.
- [10] F. Marques, M. Balcerzak, F. Winkelmann, G. Zepon, M. Felderhoff, Review and outlook on high-entropy alloys for hydrogen storage, *Energy Environ. Sci.* 14 (2021) 5191–5227, <https://doi.org/10.1039/dtee01543e>.
- [11] E. Halpren, X. Yao, Z.W. Chen, C.V. Singh, Machine learning assisted design of BCC high entropy alloys for room temperature hydrogen storage, *Acta Mater.* 270 (2024), <https://doi.org/10.1016/j.actamat.2024.119841>.

- [12] P. Zhou, Q. Zhou, X. Xiao, X. Fan, Y. Zou, L. Sun, et al., Machine learning in solid-state hydrogen storage materials: challenges and perspectives, *Adv. Mater.* 37 (2025), <https://doi.org/10.1002/adma.202413430>.
- [13] S. Xia, W. Yang, Y. Zhang, Prediction of the optimal hydrogen storage in high entropy alloys, *Mater. Chem. Phys.* 328 (2024), <https://doi.org/10.1016/j.matchemphys.2024.130010>.
- [14] H. Shen, J. Hu, P. Li, G. Huang, J. Zhang, J. Zhang, et al., Compositional dependence of hydrogenation performance of Ti-Zr-Hf-Mo-Nb high-entropy alloys for hydrogen/tritium storage, *J. Mater. Sci. Technol.* 55 (2020) 116–125, <https://doi.org/10.1016/j.jmst.2019.08.060>.
- [15] J. Wang, P. Zhou, Y. Jia, J. Feng, J. Qi, F. Chu, et al., Binding energy crossover mechanism enables low-temperature hydrogen storage performance of dual-phase TiZrCrMnNi(VFe) high-entropy alloy, *Chem. Eng. J.* 502 (2024), <https://doi.org/10.1016/j.cej.2024.157871>.
- [16] K.B. Park, J.Y. Park, Y. Kim, Do, J.I. Choi, H.T. Im, J.W. Kang, et al., Study on hydrogen absorption and surface properties of TiZrVNbCr high entropy alloy, *Intermetallics* 130 (2021), <https://doi.org/10.1016/j.intermet.2020.107074>.
- [17] F. Marques, M. Balcerzak, F. Winkelmann, G. Zepon, M. Felderhoff, Review and outlook on high-entropy alloys for hydrogen storage, *Energy Environ. Sci.* 14 (2021) 5191–5227, <https://doi.org/10.1039/dlee01543e>.
- [18] F. Yang, J. Wang, Y. Zhang, Z. Wu, Z. Zhang, F. Zhao, et al., Recent progress on the development of high entropy alloys (HEAs) for solid hydrogen storage: a review, *Int. J. Hydrot. Energy* 47 (2022) 11236–11249, <https://doi.org/10.1016/j.ijhydene.2022.01.141>.
- [19] L. Luo, L. Chen, L. Li, S. Liu, Y. Li, C. Li, et al., High-entropy alloys for solid hydrogen storage: a review, *Int. J. Hydrot. Energy* 50 (2024) 406–430, <https://doi.org/10.1016/j.ijhydene.2023.07.146>.
- [20] H. Hashimoto, S. Isobe, N. Hashimoto, H. Oka, Synthesis of Li-Mg-Al-Ti based lightweight high entropy alloys by mechanical alloying and investigation of conditions for solid solution formation, *J. Alloy. Metall. Syst.* 4 (2023) 100037, <https://doi.org/10.1016/j.jalmes.2023.100037>.
- [21] L.-c Ming, M.H. Manghnani, K.W. Katahara, Phase transformations in the Ti-V system under high pressure up to 25 GPa, *Acta Metall.* 29 (1981) 479–485, [https://doi.org/10.1016/0001-6160\(81\)90071-7](https://doi.org/10.1016/0001-6160(81)90071-7).
- [22] D.W. Levinson, On the lattice parameter of Mg-Li β alloys, *Acta Metall.* 3 (1955) 294–295, [https://doi.org/10.1016/0001-6160\(55\)90069-9](https://doi.org/10.1016/0001-6160(55)90069-9).
- [23] T. Kimura, H. Miyaoka, T. Ichikawa, Y. Kojima, Hydrogen absorption of catalyzed magnesium below room temperature, *Int. J. Hydrot. Energy* 38 (2013) 13728–13733, <https://doi.org/10.1016/j.ijhydene.2013.08.043>.
- [24] M. Peška, T. Czujko, M. Polański, Hydrogenation ability of Mg-Li alloys, *Energies* 13 (2020), <https://doi.org/10.3390/en13082080>.
- [25] Y. Fukai, 2005, The Metal-Hydrogen System, Vol. 21, Springer Berlin HeidelbergBerlin, Heidelberg, 10.1007/3-540-28883-X.
- [26] E. Veleckis, E.H. Van Deventer, M. Blander, Lithium-lithium hydride system, *J. Phys. Chem.* 78 (1974) 1933–1940, <https://doi.org/10.1021/j100612a013>.
- [27] M. Peška, A. Dębski, W. Gaśior, S. Dyjak, W. Gierlotka, A. Baran, et al., Hydrogenation behavior of Mg-Li alloys, *ACS Appl. Energy Mater.* (2025), <https://doi.org/10.1021/acsaem.4c02396>.
- [28] Y. Shang, Z. Lei, E. Alvares, S. Garroni, T. Chen, R. Dore, et al., Ultra-lightweight compositionally complex alloys with large ambient-temperature hydrogen storage capacity, *Mater. Today* 67 (2023) 113–126, <https://doi.org/10.1016/j.mattod.2023.06.012>.
- [29] K.R. Cardoso, V. Roche, A.M. Jorge, F.J. Antequira, G. Zepon, Y. Champion, Hydrogen storage in MgAlTiFeNi high entropy alloy, *J. Alloy. Compd.* 858 (2021), <https://doi.org/10.1016/j.jallcom.2020.158357>.
- [30] R.B. Strozi, D.R. Leiva, J. Huot, W.J. Botta, G. Zepon, An approach to design single BCC Mg-containing high entropy alloys for hydrogen storage applications, *Int. J. Hydrot. Energy* 46 (2021) 25555–25561, <https://doi.org/10.1016/j.ijhydene.2021.05.087>.
- [31] J. Montero, G. Ek, M. Sahlberg, C. Zlotea, Improving the hydrogen cycling properties by mg addition in Ti-V-Zr-Nb refractory high entropy alloy, *Scr. Mater.* 194 (2021), <https://doi.org/10.1016/j.scriptamat.2020.113699>.
- [32] R.B. Strozi, D.R. Leiva, J. Huot, W.J. Botta, G. Zepon, Synthesis and hydrogen storage behavior of Mg–V–Al–Cr–Ni high entropy alloys, *Int. J. Hydrot. Energy* 46 (2021) 2351–2361, <https://doi.org/10.1016/j.ijhydene.2020.10.106>.
- [33] M.O. de Marco, Y. Li, H.W. Li, K. Edalati, R. Floriano, Mechanical synthesis and hydrogen storage characterization of MgVCr and MgVTiCrFe High-Entropy alloy, *Adv. Eng. Mater.* 22 (2020), <https://doi.org/10.1002/adem.201901079>.
- [34] G. Zepon, D.R. Leiva, R.B. Strozi, A. Bedoch, S.J.A. Figueroa, T.T. Ishikawa, et al., Hydrogen-induced phase transition of MgZrTiFe_{0.5}Co_{0.5}Ni_{0.5} high entropy alloy, *Int. J. Hydrot. Energy* 43 (2018) 1702–1708, <https://doi.org/10.1016/j.ijhydene.2017.11.106>.
- [35] M. de Ferraz, W.J. Botta, G. Zepon, Synthesis, characterization and first hydrogen absorption/desorption of the Mg₃₅Al₁₅Ti₂₅V₁₀Zn₁₅ high entropy alloy, *Int. J. Hydrot. Energy* 47 (2022) 22881–22892, <https://doi.org/10.1016/j.ijhydene.2022.05.098>.
- [36] N. Pineda-Romero, C. Zlotea, Uncovering the effect of al addition on the hydrogen storage properties of the ternary TiVNb alloy, *Materials* 15 (2022), <https://doi.org/10.3390/ma15227974>.
- [37] S. Kumar, P.K. Singh, Y. Kojima, V. Kain, Cyclic hydrogen storage properties of V-Ti-Cr-Al alloy, *Int. J. Hydrot. Energy* 43 (2018) 7096–7101, <https://doi.org/10.1016/j.ijhydene.2018.02.103>.
- [38] Y. Yan, Y. Chen, H. Liang, C. Wu, M. Tao, T. Mingjing, Effect of al on hydrogen storage properties of V₃₀Ti₃₅Cr₂₅Fe₁₀ alloy, *J. Alloy. Compd.* 426 (2006) 253–255, <https://doi.org/10.1016/j.jallcom.2005.12.122>.